From Image to Insight: Optimized Multiplex Staining Panel for FFPE Mouse Bone Marrow Enables Spatial Profiling of the Hematopoietic Niche

Franziska Zell , Katharina Gellrich , Albert Gründer , Jana Schulze , Anja Müller , Philipp Eble , Fiona Preiß , Annika Grafemeyer , Christoph Koellerer , Anne Marie Staehle , Sarolta Bojtine Kovacs , Sofia Kovalchuk , Elias Erny , Catarina Reis Orcinha , Lena Illert , Heike L. Pahl , Hans Felix Staehle

PII: S0301-472X(26)00052-4
DOI: https://doi.org/10.1016/j.exphem.2026.105419
Reference: EXPHEM 105419

To appear in: *Experimental Hematology*

Received date: 15 January 2026
Revised date: 10 March 2026
Accepted date: 12 March 2026

Please cite this article as: Franziska Zell , Katharina Gellrich , Albert Gründer , Jana Schulze , Anja Müller , Philipp Eble , Fiona Preiß , Annika Grafemeyer , Christoph Koellerer , Anne Marie Staehle , Sarolta Bojtine Kovacs , Sofia Kovalchuk , Elias Erny , Catarina Reis Orcinha , Lena Illert , Heike L. Pahl , Hans Felix Staehle , From Image to Insight: Optimized Multiplex Staining Panel for FFPE Mouse Bone Marrow Enables Spatial Profiling of the Hematopoietic Niche, *Experimental Hematology* (2026), doi: https://doi.org/10.1016/j.exphem.2026.105419

From Image to Insight: Optimized Multiplex Staining Panel for FFPE Mouse Bone Marrow Enables Spatial Profiling of the Hematopoietic Niche

Franziska Zell,[1] Katharina Gellrich,[1] Albert Gründer,[1] Jana Schulze,[1,2] Anja Müller,[1] Philipp Eble,[1] Fiona Preiß,[1] Annika Grafemeyer,[1] Christoph Koellerer,[1] Anne Marie Staehle,[1] Sarolta Bojtine Kovacs,[1] Sofia Kovalchuk,[1] Elias Erny,[3] Catarina Reis Orcinha,[1,4,5] Lena Illert,[1,6] Heike L. Pahl,[1] Hans Felix Staehle[1*]

[1]Division of Molecular Hematology, Department of Medicine I, Medical Center – University of Freiburg, Faculty of Medicine, University of Freiburg, Freiburg, Germany

[2]Faculty of Biology, University of Freiburg, Freiburg, Germany

[3]Institute of Experimental and Clinical Pharmacology and Toxicology, Faculty of Medicine, University of Freiburg, Freiburg, Germany

[4]German Cancer Consortium (DKTK), Partner site Freiburg - a partnership between German Cancer Research Center (DKFZ) and Medical Center, University of Freiburg, Freiburg, Germany

[5]Current: Institute for Experimental Cardiovascular Medicine, University Heart Center Freiburg – Bad Krozingen, Medical Faculty and Medical Center, University of Freiburg, Freiburg, Germany

[6]Division of Hematology and Medical Oncology, Department of Medicine, Medical Center – Georg-August University Göttingen, Faculty of Medicine, Göttingen, Germany

***Corresponding Author:**

Hans Felix Staehle

Phone: +49-761-270-71800

Fax: +49-761-270-63410

E-mail: hans.felix.staehle@uniklinik-freiburg.de

Postal address: Zentrum Translationale Zellforschung, Breisacher Str. 115, 79106 FR, Germany

Category for the Table of Contents: New Techniques and Technologies

Word count (Abstract, Introduction, Results, Discussion): 3640

Keywords: Multiplex Immunohistochemistry; Bone marrow microenvironment; Imaging-based analysis; Spatial profiling; FFPE tissue; Murine bone marrow; JAK2V617F mouse model; Hematopoietic stem and progenitor cells; Megakaryocytic niche

Abstract

Cellular composition and spatial architecture of the bone marrow niche play a critical role in regulating both normal and malignant hematopoiesis. While flow cytometry enables rapid analysis of hematopoietic and niche cell composition, it requires single-cell dissociation, thereby disrupting the spatial context. In contrast, immunofluorescence imaging preserves tissue architecture but is limited in the number of markers that can be simultaneously detected. Recent advances in multiplex staining technologies now permit visualization of numerous antigens within a single tissue section, providing a more comprehensive view of the bone marrow microenvironment. Despite the central role of murine models in studying hematopoiesis, validated multiplex panels for analyzing murine bone marrow remain limited. This is particularly true for formalin-fixed, paraffin-embedded (FFPE) sections, where challenges such as high autofluorescence and tissue damage during antigen retrieval place substantial demands on tissue preparation. In this study, we optimized tissue preparation for staining murine FFPE bone marrow and developed an efficient multiplex immunohistochemistry panel for detecting hematopoietic stem cell-containing populations within their native niche architecture. Applying our panel to FFPE bone marrow sections from $Jak2^{V617F}$ mice revealed alterations in the megakaryocytic niche, demonstrating the utility of this approach for characterizing disease-associated spatial changes within the hematopoietic microenvironment.

Introduction

Studying the interactions between hematopoietic cells (HSCs) and their niche is essential for understanding both normal and malignant hematopoiesis.[1,2] Flow cytometry is an established technique that enables rapid and efficient analysis of both hematopoietic and niche cells. However, because it requires single cell dissociation, the spatial organization of the bone marrow is lost.[3] In contrast, immunofluorescence preserves the spatial context, allowing detection of cells *in situ*, but it is typically limited to the simultaneous use of only a few markers.[4] To address this limitation, novel multiplex imaging technologies have emerged that support spatial analysis of a larger number of markers such as co-detection by indexing (CODEX) and multiplex immunohistochemistry (mIHC).[5,6]

In CODEX, tissue sections are simultaneously stained with a large panel of DNA-barcoded antibodies.[6] During iterative imaging cycles, sets of typically three fluorescently labeled oligonucleotide probes, complementary to the DNA barcodes, are sequentially added and then washed away. This process is repeated until all targets have been visualized, enabling the detection of dozens and, theoretically, even hundreds of markers within a single tissue section. However, CODEX is highly cost-intensive and requires time-consuming panel preparation and optimization, particularly when visualizing proteins for which barcoded antibodies are not commercially available.

Compared to CODEX, mIHC is significantly more cost-effective and allows detection of up to seven markers per section. Commercially available mIHC kits from Akoya Biosciences are based on the principle of tyramide signal amplification (TSA).[7,8] In successive staining cycles, unconjugated primary antibodies bind their targets and are detected by HRP-conjugated secondary antibodies, which catalyze the covalent binding of fluorescently labeled tyramide substrates (Opal dyes) to the tissue near the antigen site. The antibodies are then removed by heat-induced stripping, and the cycle is repeated with a new target and a distinct Opal dye. Spectrally optimized panels enable reliable spectral unmixing, allowing clear allocation of signals to specific targets. Furthermore, TSA-based signal amplification enables sensitive detection of targets with low expression levels. mIHC therefore represents a robust and cost-effective alternative to the high-plex systems, one that enables rapid customization of staining panels composed of up to seven targets or markers.

While mouse models constitute an indispensable tool for studying both healthy and malignant hematopoiesis, reliable multiplex panels for analyzing murine bone marrow remain limited.[9,10] Recently, Karnik et al.[11] optimized a CODEX-based multiplex panel for staining hematopoietic cells in murine bone marrow. Due to the lack of pre-conjugated antibodies for formalin-fixed, paraffin-embedded (FFPE) murine tissue, high levels of autofluorescence, and the requirement for antigen retrieval, they chose to develop their panel using cryosectioning rather than FFPE tissue. Nevertheless, FFPE tissue offers several advantages: (i) superior preservation of tissue morphology; (ii) long-term, low-maintenance storage; and (iii) easier sectioning, enabling thinner slices with reduced cellular overlap compared to cryosections.[12,13]

To overcome the challenges associated with FFPE sections, we optimized mIHC staining for murine bone marrow and established an efficient panel that enables the identification of HSC-containing cell populations within the context of essential niche structures on murine FFPE sections.

Results

Optimized Tissue Preparation for Immunofluorescence and Multiplex Immunohistochemistry Staining on Murine FFPE Bone Marrow Sections

To enable visualization, quantification, and spatial analysis of key bone marrow niche components, we established an optimized workflow for immunofluorescence (IF) and multiplex immunohistochemistry (mIHC) staining on FFPE bone marrow sections (**Fig. 1**).

In an initial series of experiments, we used classical IF with single antigen staining to optimize various parameters, prior to multiplexing. First, we evaluated the effect of section thickness on staining quality. Bone marrow sections of 2, 3, 5, and 10 µm were stained with DAPI as well as an antibody against c-Kit (**Fig. 2A**). Sections with a thickness of 2-3 µm provided high cellular resolution, while sections at 5 and 10 µm exhibited signal overlap between adjacent cells. Although the 2 µm sections offered excellent resolution, they frequently developed fissures, compromising tissue integrity. In contrast, sections ranging from 3 to 10 µm better preserved tissue morphology. Based on these findings, we determined that 3 µm sections provided the optimal balance between cellular resolution and structural preservation, and this thickness was used in all subsequent experiments (**Fig. 2B**).

We next assessed autofluorescence levels in murine bone marrow sections. Compared to other tissues, bone marrow contains high levels of endogenous autofluorescent compounds such as hemoglobin, flavin adenine dinucleotide (FAD), collagen, and lipofuscin.[14–17] In addition, formalin fixation induces Schiff base formation, and paraffin itself exhibits intrinsic autofluorescence, both of which contribute to non-specific background signal.[18,19] In FFPE sections from wild-type mice stained only with DAPI, we observed strong autofluorescence, with the most intense signal in the green light spectrum, detected around 525 nm (**Fig. 3A**, left). Predictably, this background signal interfered with the detection of c-Kit marked by Alexa Fluor 488 (**Fig. 3A**, right). Since GFP is widely used as a detection marker in many mouse models, we also evaluated background signal in *UBC-GFP* transgenic mice, which express GFP

under the control of the human ubiquitin C (UBC) promoter, to mimic the presence of GFP expression. In FFPE sections from these mice, intrinsic GFP fluorescence is largely lost due to protein denaturation during tissue processing, requiring detection with an anti-GFP antibody. However, residual and only partially degraded GFP still contributes to non-specific background signal in these mice (**Fig. 3B**). To reduce both, autofluorescence and residual GFP signals, we applied a photobleaching protocol using high-intensity LED light.[20] This treatment effectively reduced non-specific background noise, enabling specific signal detection (**Fig. 3C+D**).

Having established optimal sectioning conditions and reduced background fluorescence, we next focused on improving antigen retrieval to enhance signal intensity. Antigen retrieval is essential to unmask epitopes obscured by protein cross-linking during formalin fixation. To modulate antigen retrieval strength, FFPE bone marrow sections, fixed overnight and embedded in paraffin, were pressure-cooked for 5, 10 or 15 minutes in a Tris-EDTA pH 9 antigen retrieval buffer (**Fig. 4A**). As anticipated, increased retrieval time enhanced staining intensity (**Fig. 4A+B**). However, antigen retrieval times longer than 5 minutes resulted in detachment of the compact bone layer, even when using SuperFrost® plus slides (**Fig. 4A+B**). To preserve tissue architecture while maintaining strong signal intensity, we reduced the fixation time (**Fig. 4C**). Shorter fixation minimized protein cross-linking, allowing efficient epitope exposure with milder retrieval conditions (**Fig. 4C+D**). Based on these findings, all subsequent experiments were performed using a 2-hour fixation and 5-minute antigen retrieval.

The efficiency of antigen retrieval is also influenced by the pH of the buffer and this parameter must be optimized individually for each antibody. Buffers at pH 6 (e.g., sodium citrate) are considered to promote mild antigen retrieval and to unmask easily accessible epitopes with minimal tissue stress, whereas buffers at pH 9 (e.g., Tris-EDTA) provide more aggressive conditions capable of exposing heavily masked antigens.[21] To determine optimal conditions for our bone marrow niche antibody panel, we compared buffers at pH 6 and pH 9 for each antibody individually (c-Kit, Sca1, GFP, CD41, and endomucin, **Fig. 5**). Retrieval at pH 9 consistently resulted in stronger signals, while preserving tissue morphology. Based on these findings, all subsequent stainings were conducted at pH 9.

Multiplex Immunohistochemistry Staining Detects Key Components of the Murine Bone Marrow Niche in FFPE Sections

Having established optimized staining conditions for antibodies targeting key components of the bone marrow niche in FFPE sections, we next combined them into a single panel for multiplex immunohistochemistry staining using the Opal multiplex technology (Akoya Biosciences, **Fig. 6A, Suppl. Fig. 1**). Our panel includes c-Kit and Sca1 to identify hematopoietic stem and progenitor cells (HSPCs). Sca1 is also expressed on arterioles, which represent an essential component of the vascular niche.[22] We tested two different Sca1 antibody clones and found that clone EPR3355 was better suited for detecting hematopoietic cells, while clone E13-161.7 produced a stronger signal on arterioles (**Suppl. Fig. 2**). Both clones were therefore included in the panel. In addition, the panel includes antibodies against CD41 and endomucin to identify megakaryocytes and sinusoidal endothelial cells, respectively. An anti-GFP antibody was included to enable detection of GFP-labeled cells, and DAPI was used for nuclear staining.

We first tested our panel on bone marrow sections from lethally irradiated mice transplanted with donor cells derived from *UBC-GFP* mice (**Fig. 6**). In this model, GFP serves as a marker for donor-derived hematopoietic cells. After image acquisition, raw images were processed to enable accurate data analysis (**Fig. 6A-C**). Processing involved spectral unmixing within a defined region of interest to separate overlapping fluorescence signals that occur during the acquisition process. Cleared images were then used for data analysis, which was divided into three steps (**Suppl. Fig. 3A**): (i) Cell detection was used to identify cells of interest within the niche environment. (ii) Tissue detection was applied to mark components of the niche, which often exhibit more complex structures. (iii) Spatial analysis was performed to determine the distance between the niche and the cells residing within it.

In our panel, cell detection was used to identify $DAPI^+$, GFP^+, c-Kit^+, and $Sca1^+$ cells, and to calculate their respective cell densities within the region of interest (**Fig. 6D,E; Suppl. Fig. 3B; Suppl. Fig. 4**). Nuclear staining with DAPI enabled an approximation of the total cell number and density, revealing an average of approximately 19,000 cells/mm^2 (**Suppl. Table 1**). In the analyzed tissue sections—obtained from mice transplanted with donor cells from *UBC-GFP* mice—the number of GFP^+ cells closely matched the total cell count determined by DAPI staining, indicating efficient engraftment of the donor cells, which was also verified by FACS analysis (**Suppl. Fig. 5**). We further analyzed the c-Kit^+ and c-Kit^+/$Sca1^+$ populations,

representing HSPCs and HSCs, respectively. We found that 7.7% of cells were c-Kit$^+$ and 0.9% were c-Kit$^+$/Sca1$^+$ (**Fig. 6F**, **Suppl. Table 1**). In addition, we calculated the average cell size in these populations, both depicting a similar diameter of approximately 10 µm (**Fig. 6G**).

Importantly, each staining cycle of the mIHC protocol results in progressive cell loss, with approximately 20% of cells lost after six staining rounds (**Suppl. Fig. 6**). Consequently, when comparing tissue sections subjected to different numbers of staining cycles, only the relative frequencies of cell populations can be evaluated, whereas direct comparisons of absolute cell counts are not informative.

Bone marrow niche components were detected either through machine learning-based tissue analysis or by manual annotation (**Suppl. Fig. 3A**). The machine learning approach was applied to identify CD41$^+$ megakaryocytes and endomucin$^+$ sinusoids (**Fig. 6H; Suppl. Fig. 3C, Suppl. Fig. 4**), while manual annotation was used to mark Sca1$^+$ arterioles and the endosteal bone surface (**Suppl. Fig. 3D**). Analysis of these structures revealed that approximately 13% of the selected area was covered by sinusoids, whereas arterioles accounted for less than 1% (**Fig. 6I**). Additionally, in these mice transplanted with donor cells from *UBC-GFP* mice we identified an average of 82 megakaryocytes per mm^2, with an average cell size of 21.2 µm (**Fig. 6J+K**).

Having identified the cells of interest within the niche, we next quantified their spatial relationships to key niche components (**Suppl. Fig. 3E**). c-Kit$^+$/Sca1$^+$ cells were most closely associated with sinusoids, followed by megakaryocytes, whereas fewer cells were located near arterioles and the endosteal bone surface (**Fig. 6L–N**). According to Francis et al.[23] and Handly et al.[24], paracrine signaling can influence cells within a range of up to 100 µm, although its efficacy diminishes with increasing distance. We found that > 90% of the c-Kit$^+$/Sca1$^+$ cells were located within 100 µm of sinusoids and megakaryocytes, whereas only approximately 25% of the c-Kit$^+$/Sca1$^+$ cells were within 100 µm of arterioles or the endosteal surface (**Suppl. Fig. 7A**). When applying a more stringent cutoff of 25 µm, 66% of c-Kit$^+$/Sca1$^+$ cells remained within this distance to sinusoids, 24% within 25 µm to megakaryocytes, and only ~6% were within 25 µm to arterioles or the endosteal bone surface (**Suppl. Fig. 7B**).

To demonstrate the adaptability and full capacity of our approach, we performed a seven-marker staining using the core markers DAPI, c-Kit, Sca1, CD41, and endomucin, combined with the granulocyte marker Gr-1 and the B cell marker B220 (**Suppl. Fig. 8**). In addition, our

tissue preparation protocol was also transferable to other skeletal sites, including tibiae, pelves, vertebrae, and humeri (**Suppl. Fig. 9**).

In summary, our panel enables the determination of both the frequency and size of cells of interest in FFPE bone marrow, as well as their spatial location and distance to sinusoidal, arteriolar, megakaryocytic, and endosteal niche cells.

Jak2^{V617F} mice display an altered megakaryocytic bone marrow niche

To test whether our panel detects changes associated with aberrant hematopoiesis, we applied it to bone marrow sections derived from a well-established Jak2^{V617F} mouse model (**Fig. 7A+B**).[25] At the time of analysis, the disease phenotype was fully established as the animals demonstrated trilineage myeloproliferation accompanied by splenomegaly (**Suppl. Fig. 10**). As previously shown in the literature, Jak2^{V617F} mice exhibited a marked increase in the number of c-Kit$^+$ and c-Kit$^+$/Sca1$^+$ cells compared to wild-type littermate controls (**Fig. 7C, Suppl. Table 1**). To validate our measurements, we compared the frequencies of c-Kit$^+$ and c-Kit$^+$/Sca1$^+$ cells obtained using the Akoya-based imaging approach with those determined by flow cytometry (**Suppl. Fig. 11**). Both methods yielded comparable results, supporting the validity and robustness of our panel.

We observed a significant increase in both the abundance and the average size of megakaryocytes in Jak2^{V617F} mice (**Fig. 7D+E, Suppl. Table 1**). Consequently, megakaryocytes occupy a larger area of the bone marrow in these animals (**Fig. 7F**). In addition, the area covered by sinusoids was significantly expanded in Jak2^{V617F} mice, whereas the abundance of arterioles remained unchanged (**Fig. 7F**). Quantification of the distance between c-Kit$^+$/Sca1$^+$ cells and niche cells revealed that the Jak2^{V617F} mutation did not affect the proximity of these cells to sinusoids (**Fig. 7G**), arterioles or the endosteal bone surface (**Fig. 7H+I**). In contrast, c-Kit$^+$/Sca1$^+$ cells were found to be significantly closer to megakaryocytes in Jak2^{V617F} mice compared to littermate controls (**Fig. 7J-L**). However, when we measured the distance of randomly assigned DAPI-labeled cells to megakaryocytes in JAK2^{V617F} mice, we also observed a closer proximity, indicating that this effect largely arises from the higher megakaryocyte density rather than from a specific localization of Kit$^+$/Sca1$^+$ cells close to megakaryocytes (**Suppl. Fig. 12**).

Discussion

Multiplex spatial imaging is gaining increasing importance as the pivotal contribution exerted by the microenvironment in modulating cell identity and cell state is increasingly being recognized. Hence, staining panels and protocols for various human tissue types have recently been published.[9,26–28] However, the preparation and staining of bone marrow poses a particular challenge. The rigid bone structure requires decalcification prior to processing, and preserving tissue integrity during sectioning and antigen retrieval remains difficult. Additionally, the soft bone marrow is densely packed with heterogeneous blood cells that exhibit high autofluorescence and lie in close spatial proximity, often making it difficult to clearly distinguish signals from individual cells.[14–17,29]

Walters et al.[9] established a multiplex staining protocol that enables the identification of myeloma cells, T cells, and macrophages in FFPE human bone marrow. However, in contrast to human bone marrow core biopsies, which primarily consist of spongiosa, murine femora are completely encased in compact bone, placing greater demands on tissue preparation and processing. Recently, Karnik et al.[11] described a CODEX-based protocol for detecting HSPCs in the murine bone marrow niche. However, due to the challenges associated with FFPE sections, including high autofluorescence and tissue damage during antigen retrieval, cryosections were used in this study.

To overcome the challenges associated with FFPE sections, we optimized tissue preparation and antigen retrieval for murine femora (**Fig. 4+5**). By incorporating a highly effective photobleaching protocol we nearly eliminated non-specific background signals (**Fig. 3**) resulting in a protocol that enables high-quality multiplex staining of murine FFPE bone marrow sections. The panel utilizes five markers, c-Kit, Sca1, endomucin, CD41, and DAPI, and can be extended with up to two additional markers, depending on the specific research question (**Suppl. Fig. 9**).

Our approach enables robust analysis of bone marrow niche architecture and is particularly well-suited for addressing defined biological questions in a time- and cost-efficient manner. For applications requiring the simultaneous detection of more than seven markers, alternative multiplexing technologies such as CODEX are available. However, in the context of murine

bone marrow, CODEX has so far been established only for cryosections. Our optimized protocol for FFPE tissue preparation may facilitate the development of a CODEX-compatible staining method for murine FFPE bone marrow sections, representing a promising next step toward advancing the characterization of the bone marrow niche.

While our mIHC protocol and the CODEX panel described by Karnik et al.[11] focus on single-cell resolution in relatively thin sections (3–10 µm), other techniques enable spatial analysis of substantially thicker bone specimens. Recently, Wu et al. established a whole-mount approach in which freshly fixed bone sections were stained with up to four markers, enabling reliable confocal imaging at depths of up to 35 µm. A key advantage of this technique is the improved visualization of in situ cellular interactions within the niche in a three-dimensional context. In addition, Mertens et al. developed a multistep clearing protocol that enabled three-dimensional analysis of an entire mouse femur. Using this approach, signals could be detected at depths of up to 400 µm within the tissue. However, this protocol likewise depends on fresh material and remains limited with respect to multiplexing capacity. Thus, depending on the specific requirements of a given experiment, such as tissue preparation, spatial resolution, and multiplexing capacity, an increasing number of staining protocols for murine bone are currently available (**Table 1**).

Our staining panel allows the detection of c-Kit$^+$/Sca1$^+$ cells in spatially preserved murine bone marrow (**Fig. 6+7**). Ogawa et al.[32] and Chatterjee et al.[33] investigated the frequencies of c-Kit$^+$ and Sca1$^+$ cells in murine bone marrow using flow cytometry and reported 7.8% and 21%, respectively. Similarly, Kyle-Cezar et al.[34] found frequencies of 4.19% for c-Kit$^+$, 9.30% for Sca1$^+$, and 0.89% for c-Kit$^+$/Sca1$^+$ cells by FACS analysis. Our staining panel yields comparable results, detecting 7.66% c-Kit$^+$, 15.30% Sca1$^+$, and 0.89% c-Kit$^+$/Sca1$^+$ cells in mice transplanted with *UBC-GFP* donor cells (**Suppl. Table 1**). Moreover, we quantitated the increased frequency of c-Kit$^+$/Sca1$^+$ cells in JAK2^{V617F} mice in parallel by multiplex staining on FFPE bone marrow and by FACS and obtained very similar results.

Using our panel, we identified 0.42% CD41$^+$ megakaryocytes with an average diameter of 21.2 µm in mice transplanted with *UBC-GFP* donor cells (**Fig. 6K, Suppl. Table 1**). These findings are consistent with flow cytometry-based reports of murine bone marrow by Spindler et al.[35]

and Corash et al.[36], who observed megakaryocyte frequencies of 0.4% and 0.14%, respectively. Furthermore, Gorelashvili et al.[37] reported an average megakaryocyte size of 25 µm, closely aligning with our observations.

Our panel also enables the detection of bone marrow vasculature. We observed that endomucin$^+$ sinusoids occupied approximately 13% of the bone marrow area in mice transplanted with *UBC-GFP* donor cells (**Fig. 6I**). In comparison, endomucin$^+$ sinusoids constituted around 20% of the area in murine femoral sections in a study by Gomariz et al.[38] Our spatial analysis further revealed that nearly all c-Kit$^+$/Sca1$^+$ cells were located within 100 µm of a sinusoid, with 66% residing within 25 µm (**Suppl. Fig. 8**). This observation is also consistent with previously reported distributions of HSCs in proximity to the sinusoidal niche.[39]

When applying our staining panel to Jak2^{V617F} mice, we were able to recapitulate three previously reported characteristics: the expansion of c-Kit$^+$/Sca1$^+$ cells[25,40] as well as the increase in the number of enlarged megakaryocytes and the expansion of the sinusoidal vascular network (**Fig. 7**).[41–45]

Because of the enlarged megakaryocytes, all other bone marrow cells, including c-Kit$^+$/Sca1$^+$ cells are located closer to megakaryocytes in Jak2^{V617F} mice compared to littermate controls (**Fig. 7J**). The megakaryocytic niche is postulated to promote HSC quiescence via the secretion of transforming growth factor beta 1 (TGF-β1), thrombopoietin (TPO), and C-X-C motif chemokine ligand 4 (CXCL4), thereby preserving stem cell dormancy and protecting HSCs from exhaustion and apoptosis.[39,46–49] This observation aligns with the findings of Zhang et al.[48], who showed that megakaryocyte-derived TPO maintains HSC quiescence in a Jak2^{V617F} model. Jak2^{V617F}-mediated myeloproliferation is accompanied by increased oxidative stress and inflammation, which may necessitate enhanced vascular support and a more protective microenvironment for HSCs.[50–52] In line with this model, we observed increased vascularization in Jak2^{V617F} bone marrow (**Fig. 7F+J**). These findings suggest that an expanded megakaryocytic niche and vascular network in Jak2^{V617F} mice might facilitate the maintenance of a quiescent malignant HSPC pool under conditions of chronic proliferative and inflammatory stress.

In summary, although many studies include bone marrow immunofluorescence staining, there is currently no published standardized and structured workflow for murine FFPE bone marrow sections, which we present in this work. Moreover, we developed a time- and cost-effective multiplex panel to stain key components of the murine bone marrow niche that can be readily adapted to individual research questions.

Materials and Methods

Generation of Jak2^{V617F} mice

Floxed *Jak2* ki mice were crossed with *Mx1Cre* mice to generate double transgenic mice as previously described.[53] These mice, henceforth called Jak2^{V617F} mice, express the Cre recombinase under the control of the *Mx1* promoter and carry a wildtype (WT) *Jak2^{WT}* as well as a floxed mutated *Jak2^{V617F}* allele. Cre expression was induced by poly(I:C) injections. Cre causes DNA recombination at the flox sites, leading to expression of the heterozygous Jak2^{V617F} allele. Experiments were performed with Jak2^{V617F} mice and littermate controls.

Generation of Transgenic *UBC-GFP* mice

Transgenic *UBC-GFP* mice (C57BL/6-Tg(*UBC-GFP*)30Scha/J) were first described by Schaefer et al.[54] and kindly provided by Radek Skoda. These mice ubiquitously express GFP under the control of the *human ubiquitin C (UBC)* promoter and were used to establish GFP staining. To utilize GFP as an engraftment marker, we employed a transplantation model. Donor cells were isolated from the fetal liver of 13.5-day-old *UBC-GFP* mouse embryos. Transplantation of fetal liver cells is a well-established method for long-term hematopoietic reconstitution and is routinely performed in our laboratory.[55–58] Lethally irradiated (2 × 4.5 Gy) 8–9-week-old CD45.1 WT female and male mice served as recipients. Approximately 5 million fetal liver cells were transplanted per recipient via retrobulbar injection. Recipient mice were sacrificed 132-134 days post-transplantation for final analysis.

Animal Housing and Protection

Experiments conducted on mice were approved by the Environment and Consumer Protection Agency of the State of Baden-Württemberg, Germany (G20-076, G23-022, X22-09K, and X24-03K) and all methods were performed in accordance with the relevant guidelines and regulations. The study is reported in accordance with ARRIVE guidelines. Mice were

maintained under specific pathogen-free conditions at the research mouse facility of the University Medical Center Freiburg. Lighting was adjusted to the circadian rhythm of the animals. The temperature was kept between 20 and 23˚C. Mice lived in EcoFlo cages (Allentown), enriched by nesting material such as litter, tunnels and paper towels. Mice had permanent access to water and food, which was changed every week or earlier if necessary. Special training in animal care and handling (FELASA B certificate) was mandatory for all staff working with mice. Prior to the experiments, humane endpoints were determined to avoid pain and distress of the animals. In this study, all mice were sacrificed by cervical dislocation at predetermined time points prior to reaching humane endpoints.

Complete Blood Cell Counts (CBC)

Peripheral blood samples from mice were taken via puncture of retrobulbar veins with a heparin-coated capillary and collected in heparin-coated microvette tubes. Subsequent complete blood cell count analyses were performed on an Animal Blood Counter Plus (Scil Vet).

Flow cytometry

Flow cytometry experiments were performed on a BD FACS Fortessa. Stem and progenitor cells were detected by staining with a cocktail against lineage markers (BioLegend, San Diego, USA, 133313, B220, CD3, Gr1, Mac1 and Ter119) as well as staining for c-Kit (Thermo Scientific, Waltham, USA, 47-1171-82, clone 2B8), Sca1 (BioLegend, 108120, clone D7), CD34 (BioLegend, 152205, clone SA376A4), Fc-γ-II/III-R (Thermo Scientific, 25-0161-82, clone 93), and Flt3 (Thermo Scientific, 12-1351-82, clone A2F10). Gating strategies were determined by fluorescence minus one staining as previously described.[59]

Fixation

Mice were sacrificed for subsequent femora preparation. Cleaned bones were transferred to a phosphate-buffered saline (PBS)-based 4% paraformaldehyde (PFA) solution (Carl Roth, 0335.1, Karlsruhe, Germany) and incubated at room temperature (RT) for 2-72 hours under rotation. Best results were achieved with 2 hours fixation (**Fig. 4**), which was therefore used henceforth. Following fixation, bones were washed three times for 5 minutes each in PBS.

Decalcification

Ethylenediaminetetraacetic acid (EDTA, Carl Roth, CN06.3) was used for decalcification. After fixation, bones were transferred to a 10% EDTA solution prepared with deionized water and incubated at 4°C for 6 days under rotation. Following decalcification, bones were washed three times for 5 minutes each in PBS. Subsequently, bones were stored at 4°C in 50% ethanol (SAV Liquid Production, ETO-5000-99-1, Flintsbach am Inn, Germany) for up to one week prior to paraffin embedding.

Paraffin Embedding

After decalcification, femora were placed into embedding cassettes (Carl Roth, K114.1) for dehydration and paraffin infiltration in a Leica TP1020 tissue processor (Leica Biosystems, Nussloch, Germany, **Suppl. Table 2**). Following these steps, the embedding cassettes with the bones were placed into embedding molds (Carl Roth, TT29.1) and covered with liquid paraffin (60°C) using a Leica EG 1150 embedding station (Leica Biosystems). An integrated cold plate was used for homogeneous solidification. The paraffin blocks were stored at 4°C.

Tissue Sectioning

Paraffin blocks were cut into thin sections ranging from 2 to 10 µm using a HM 355S microtome (Thermo Fisher Scientific) equipped with microtome blades (Feather Safety Razor, S35, Osaka, Japan). Before cutting, the paraffin blocks were cooled to -20°C. A Cool-Cut System (Thermo Fisher Scientific) was used to maintain a low temperature for optimal cutting. A Section Transfer System (Thermo Fisher Scientific) was used to transfer the sections to a 38.5°C water bath. The sections were then transferred to SuperFrost Plus™ adhesive slides (R. Langenbrinck, 03-0060, Emmendingen, Germany) and dried overnight at 37°C on a Medite OTS 40.3040 heating plate (Medite Medical, Burgdorf, Germany). The slides were stored at 4°C until further use.

Deparaffinization and Rehydration

Tissue sections were deparaffinized and rehydrated using an ST5020 Automatic Stainer (Leica Biosystems) in preparation for staining. A detailed protocol is shown in **Suppl. Table 3**. The slides were kept submerged in fluid until staining.

Hematoxylin-Eosin (H&E) Staining

After deparaffinization and rehydration, H&E staining was performed using an ST5020 Automatic Stainer (Leica Biosystems). A detailed protocol is shown in **Suppl. Table 4**. After staining, the slides were mounted with Entellan (Merck, 107961, Darmstadt, Germany) and covered with a coverslip (R. Langenbrinck GmbH, 80-2450/1).

Preparation of TBST Solution

TRIS-buffered saline containing 0.5% Tween 20 (TBST) was prepared from a 10x TRIS-buffered saline (TBS 10X) stock solution. The TBS 10X stock solution was prepared by dissolving 24.3 g of Tris (neoFroxx, 1125KG001, Einhausen, Germany) and 80.0 g of NaCl (VWR Chemicals, 27810.295, Radnor, USA) in 800 mL of deionized water. The pH was adjusted to 7.5 with HCl (VWR Chemicals, 20252.290) and the final volume was adjusted to 1 L with deionized water. To prepare the 1x TBST solution, 100 mL of the 10x TBS stock solution was diluted with 900 mL of deionized water, followed by the addition of 0.5 mL of Tween 20 (Merck, P1379).

Antigen Retrieval

Antigen retrieval was performed using either pH 6 or pH 9 antigen retrieval solution (AR600250ML or AR900250ML, respectively, Akoya Biosciences, Marlborough, USA). The 10x concentrated antigen retrieval buffer was diluted with deionized water to obtain a 1x solution, which was then poured into a Coplin staining jar (Merck, S5641). Deparaffinized and rehydrated sections were placed into the jar, which was loosely covered with aluminum foil and placed into a pressure cooker (Instant Pot, 920129**,** Ottawa, Canada) containing 800 mL of deionized water. Antigen retrieval was carried out for 5-15 minutes using the rapid cook setting. After cooking, the Coplin jar with the slides was placed on ice for 15 minutes to cool. The slides were then transferred to a staining tray (Merck, BR471400) filled with room temperature TBST, where they were kept until photobleaching or staining procedures.

Photobleaching

After antigen retrieval, tissue sections were subjected to photobleaching to reduce autofluorescence and, for *UBC-GFP* mice, to eliminate GFP signals. The slides were placed into four-well plates (Carl Roth, CNA2.1) and filled with 8 ml of a PBS-based bleaching solution (4.5% H_2O_2 and 20mM NaOH). The plates were then positioned between two 32,000 Lux LED

lamps (Wakects, Wakectsowe6zfcdqm, Shenzhen, China), as shown in **Fig. 1B**. After an initial 45-minute incubation, the bleaching solution was replaced, and the slides were incubated for another 45 minutes.

Blocking

After photobleaching, the slides were transferred to a staining tray (Merck, BR471400) and washed three times, each for 5 minutes, with TBST. The slides were then removed and placed on a paper towel. Any residual TBST surrounding the tissue section was carefully aspirated using a vacuum pump (KNF Neuberger, N 86 KT.18, Freiburg im Breisgau, Germany) connected to a 200 µL pipette tip (Starlab, S1120-8810, Hamburg, Germany), carefully avoiding contact with the tissue. The tissue area was then encircled with a PAP-Pen (Science Service, N71310-N, München, Germany). Next, 2-3 drops of Akoya diluent/block solution (Akoya Biosciences, ARD1001EA) were applied to completely cover the tissue. The slides were then incubated in a humidity chamber for 10 minutes to prevent drying.

Immunofluorescence (IF) Staining

After removing the blocking solution by gently tapping the slide, 50 µL of diluted primary antibody was applied to the tissue section. Antibodies were diluted in Akoya diluent/block solution (Akoya Biosciences, ARD1001EA), as listed in **Suppl. Table 5.** The slides were incubated overnight at 4°C in a humidity chamber. Subsequently, the slides were washed three times for 5 minutes each with TBST in the staining tray (Merck, BR471400). After removal from the tray, 50 µl of a fluorophore-conjugated secondary antibody, diluted in Akoya diluent/block solution (Akoya Biosciences, ARD1001EA) and supplemented with 0.05 µg/ml DAPI (BioLegend, 422801), was pipetted onto the tissue section. The secondary antibodies and their dilutions are listed in **Suppl. Table 5**. The slides were incubated in a humidity chamber at RT for 1 hour, protected from light. After incubation, the slides were washed three times for 5 minutes each with TBST, followed by a final 2-minute wash step in deionized water. The slides were then removed from the tray, and three drops of Fluoromount (Thermo Fisher Scientific, 00-4958-02) were applied to the stained tissue section. A coverslip (R. Langenbrinck GmbH, 80-2450/1) was placed on top and sealed with clear nail polish. The mounted slides were protected from light until imaging on a PhenoImager Fusion (Akoya Biosciences).

Akoya-based Multiplex Immunohistochemistry (mIHC) Staining

The Akoya-based multiplex staining technique involves a series of successive staining cycles, including primary antibody incubation, secondary antibody incubation, tyramide signal amplification, antibody stripping, and peroxidase inactivation (**Fig. 6A**). The panel design and the staining order of the antibodies are provided in **Suppl. Fig. 2**. The antigen retrieval procedure was conducted as described above, using a pH 9 antigen retrieval solution (Akoya Biosciences, AR900250ML) for 5 minutes. Blocking and primary antibody incubation were performed as outlined for immunofluorescence staining. After primary antibody incubation, the slides were washed three times for 5 minutes each with TBST in a staining tray (Merck, BR471400). Following this, 50 µl of a horseradish peroxidase (HRP)-conjugated secondary antibody, diluted in Akoya diluent/block solution (Akoya Biosciences, ARD1001EA) was applied to the tissue section. The secondary antibodies and their respective dilutions are listed in **Suppl. Table 5**. The slides were then incubated in a humidity chamber at RT for 20 minutes, protected from light. After incubation, the slides were washed three times for 5 minutes each with TBST. Next, the corresponding Opal dye was freshly diluted in amplification buffer as specified in **Suppl. Table 6**. The slides were removed from the tray, and 50 µl of the diluted Opal dye solution was pipetted onto the tissue section. Incubation occurred at RT for 20 minutes in a humidity chamber, protected from light, to allow tyramide signal amplification. During this amplification process, the HRP enzyme conjugated to the secondary antibody catalyzes the conversion of tyramide, which is conjugated to the fluorescent Opal dye, into a reactive radical.[60] These tyramide radicals then covalently bind tyrosine residues near the target epitope, ensuring precise and stable labeling.[61] Following tyramide signal amplification, the slides were washed three times for 5 minutes each with TBST. To proceed with the next staining cycle, antibodies from the current round were stripped from the section through an additional antigen retrieval step in pH 9 antigen retrieval solution (Akoya Biosciences, FP1490) for 5 minutes. After stripping, the slides were placed into a staining tray (Merck, BR471400) filled with water-based 3% H_2O_2 solution for 15 minutes to ensure peroxidase inactivation, thereby preventing nonspecific signals during the next staining cycle. After the final staining cycle, 30 µL of DAPI solution (2 drops of 10x Spectral DAPI (Akoya Biosciences, AR900250ML) in 1 mL TBST) was applied to each slide. After incubation at RT for 5 minutes in a humidity chamber protected from light, the slides were washed three times for 5 minutes each with TBST, followed by a final 2-minute washing step in deionized water. The

slides were then mounted and imaged using the PhenoImager Fusion (Akoya Biosciences) as described for immunofluorescence staining.

Imaging

The PhenoImager Fusion was used to image H&E, IF, and mIHC-stained tissue sections. A specific imaging protocol was applied for each staining type (H&E, IF, or mIHC). For H&E images, a brightfield protocol with a pixel resolution of 0.50 µm/pixel (20× objective) was used. IF and mIHC-stained sections were imaged using a fluorescence protocol with the Opal 7-color filter set and a pixel resolution of 0.50 µm/pixel (20× objective). DAPI was set as the reference for the focal plane. The optimal exposure time for each staining series was determined on a test section using the auto exposure function.

Data Processing and Analysis of mIHC Stainings

Quantitative Pathology TIFF (QPTIFF) files were uploaded to the Phenochart 2.0.1 slide viewer software (Akoya Biosciences). The stamp annotation tool was used to define a region of interest (**Fig. 6B**). The QPTIFF files were then imported into the inForm 3.0 image analysis software (Akoya Biosciences). Spectral unmixing was performed using synthetic spectral libraries within inForm and by removing autofluorescence through the selection of an unstained region with the Autofluorescence Picker Tool (**Fig. 6C**). Data analysis was conducted using QuPath 0.5.1 software[62] (**Suppl. Fig. 4**). For cell detection, signals from a single marker (DAPI, GFP, c-Kit, or Sca1) were assigned to cells using the Cell Detection tool. Based on the results of the single marker detection, cells positive for multiple markers were identified using the Object Classifier tool. $CD41^+$ megakaryocytes and $endomucin^+$ sinusoids were identified using the Pixel Classifier tool. $Sca1^+$ arterioles and the endosteal bone line were defined manually (**Suppl. Fig. 4D**). The average cell density, cell size, and the area covered by sinusoids and arterioles were quantified using the automatically generated detection and annotation measurements after applying the respective detection tool in QuPath. Spatial analyses were performed using the Distance to Annotations 2D tool.

Statistical analysis

Unpaired Student's *t*-tests were used to determine whether a significant ($p<0.05$) difference existed between two groups. Analyses were performed using the GraphPad Prism 10 software (GraphPad Software, Boston, USA).

Data Sharing Statement

The datasets generated during and/or analysed during the current study are available from the corresponding author on reasonable request.

References

[1] Méndez-Ferrer S, Bonnet D, Steensma DP, et al. Bone marrow niches in haematological malignancies. Nat Rev Cancer 2020;20:285–98. https://doi.org/10.1038/S41568-020-0245-2.

[2] Grockowiak E, Korn C, Rak J, et al. Different niches for stem cells carrying the same oncogenic driver affect pathogenesis and therapy response in myeloproliferative neoplasms. Nature Cancer 2023 4:8 2023;4:1193–209. https://doi.org/10.1038/s43018-023-00607-x.

[3] Cherian S, Hedley BD, Keeney M. Common flow cytometry pitfalls in diagnostic hematopathology. Cytometry B Clin Cytom 2019;96:449–63. https://doi.org/10.1002/CYTO.B.21854.

[4] Im K, Mareninov S, Diaz MFP, Yong WH. An introduction to performing immunofluorescence staining. Methods in Molecular Biology 2019;1897:299–311. https://doi.org/10.1007/978-1-4939-8935-5_26.

[5] Tan WCC, Nerurkar SN, Cai HY, et al. Overview of multiplex immunohistochemistry/immunofluorescence techniques in the era of cancer immunotherapy. Cancer Commun 2020;40:135–53. https://doi.org/10.1002/CAC2.12023.

[6] Goltsev Y, Samusik N, Kennedy-Darling J, et al. Deep Profiling of Mouse Splenic Architecture with CODEX Multiplexed Imaging. Cell 2018;174:968-981.e15. https://doi.org/10.1016/j.cell.2018.07.010.

[7] Viratham Pulsawatdi A, Craig SG, Bingham V, et al. A robust multiplex immunofluorescence and digital pathology workflow for the characterisation of the tumour immune microenvironment. Mol Oncol 2020;14:2384–402. https://doi.org/10.1002/1878-0261.12764,.

[8] Stack EC, Wang C, Roman KA, Hoyt CC. Multiplexed immunohistochemistry, imaging, and quantitation: A review, with an assessment of Tyramide signal amplification, multispectral imaging and multiplex analysis. Methods 2014;70:46–58. https://doi.org/10.1016/j.ymeth.2014.08.016.

[9] Walters DK, Jelinek DF. Multiplex Immunofluorescence of Bone Marrow Core Biopsies: Visualizing the Bone Marrow Immune Contexture. Journal of Histochemistry and Cytochemistry 2020;68:99–112. https://doi.org/10.1369/0022155419896802,.

[10] Ninkovic S, Purton LE, Harrison SJ, Quach H. Multiplex immunohistochemistry elucidates increased distance between cytotoxic T cells and plasma cells in relapsed myeloma, and identifies Lag-3 as the most common checkpoint receptor on cytotoxic T cells of myeloma patients. Haematologica 2024;109:1487–500. https://doi.org/10.3324/HAEMATOL.2023.283344,.

[11] Karnik SJ, Gulbronson C, Jordan PC, et al. Multiplex imaging of murine bone marrow using Phenocycler 2.0™: NORMAL HEMATOPOIESIS. Leukemia 2025;39. https://doi.org/10.1038/S41375-025-02596-5,.

[12] Chen X, Cho D-B, Yang P-C. Double staining immunohistochemistry. N Am J Med Sci 2010;2:241–5. https://doi.org/10.4297/NAJMS.2010.2241,.

[13] Hira VVV, de Jong AL, Ferro K, Khurshed M, Molenaar RJ, Van Noorden CJF. Comparison of different methodologies and cryostat versus paraffin sections for chromogenic immunohistochemistry. Acta Histochem 2019;121:125–34. https://doi.org/10.1016/j.acthis.2018.10.011.

[14] Whittington NC, Wray S. Suppression of Red Blood Cell Autofluorescence for Immunocytochemistry on Fixed Embryonic Mouse Tissue. Curr Protoc Neurosci 2017;81:2.28.1-2.28.12. https://doi.org/10.1002/CPNS.35,.

[15] Schnell SA, Staines WA, Wessendorf MW. Reduction of lipofuscin-like autofluorescence in fluorescently labeled tissue. Journal of Histochemistry and Cytochemistry 1999;47:719–30. https://doi.org/10.1177/002215549904700601,.

[16] Banerjee B, Miedema BE, Chandrsekhar HR. Role of basement membrane collagen and elastin in the autofluorescence spectra of the colon - PubMed. Journal of Investigative Medicine 1999;47:326–32.

[17] Viegas MS, Martins TC, Seco F, do Carmo A. An improved and cost-effective methodology for the reduction of autofluorescence in direct immunofluorescence studies on formalin-fixed paraffin-embedded tissues - PubMed. European Journal of Histochemistry 2007;51:59–66.

[18] Willingham MC. An alternative fixation-processing method for preembedding ultrastructural immunocytochemistry of cytoplasmic antigens: The GBS (glutaraldehyde-borohydride-saponin) procedure. Journal of Histochemistry and Cytochemistry 1983;31:791–8. https://doi.org/10.1177/31.6.6404984,.

[19] Davis AS, Richter A, Becker S, et al. Characterizing and Diminishing Autofluorescence in Formalin-fixed Paraffin-embedded Human Respiratory Tissue. Journal of Histochemistry and Cytochemistry 2014;62:405–23. https://doi.org/10.1369/0022155414531549,.

[20] Du Z, Lin JR, Rashid R, et al. Qualifying antibodies for image-based immune profiling and multiplexed tissue imaging. Nat Protoc 2019;14:2900–30. https://doi.org/10.1038/S41596-019-0206-Y,.

[21] Shi SR, Imam SA, Young L, Cote RJ, Taylor CR. Antigen retrieval immunohistochemistry under the influence of pH using monoclonal antibodies. Journal of Histochemistry and Cytochemistry 1995;43:193–201. https://doi.org/10.1177/43.2.7822775,.

[22] Kunisaki Y, Bruns I, Scheiermann C, et al. Arteriolar niches maintain haematopoietic stem cell quiescence. Nature 2013;502:637–43. https://doi.org/10.1038/NATURE12612,.

[23] Francis K, Palsson BO. Effective intercellular communication distances are determined by the relative time constants for cyto/chemokine secretion and diffusion. Proc Natl Acad Sci U S A 1997;94:12258–62. https://doi.org/10.1073/PNAS.94.23.12258,.

[24] Naomi Handly L, Pilko A, Wollman R. Paracrine communication maximizes cellular response fidelity in wound signaling. Elife 2015;4:e09652. https://doi.org/10.7554/ELIFE.09652.

[25] Hasan S, Lacout C, Marty C, et al. JAK2V617F expression in mice amplifies early hematopoietic cells and gives them a competitive advantage that is hampered by IFNa. Blood 2013;122:1464–77. https://doi.org/10.1182/BLOOD-2013-04-498956,.

[26] Feng Z, Bethmann D, Kappler M, et al. Multiparametric immune profiling in HPV– oral squamous cell cancer. JCI Insight 2017;2. https://doi.org/10.1172/JCI.INSIGHT.93652,.

[27] Feng Z, Puri S, Moudgil T, et al. Multispectral imaging of formalin-fixed tissue predicts ability to generate tumor-infiltrating lymphocytes from melanoma. J Immunother Cancer 2015;3. https://doi.org/10.1186/S40425-015-0091-Z,.

[28] Bauer M, Vaxevanis C, Bethmann D, et al. Multiplex immunohistochemistry as a novel tool for the topographic assessment of the bone marrow stem cell niche. Methods Enzymol 2020;635:67–79. https://doi.org/10.1016/bs.mie.2019.05.055.

[29] Le VH, Lee S, Lee S, et al. In vivo longitudinal visualization of bone marrow engraftment process in mouse calvaria using two-photon microscopy. Sci Rep 2017;7. https://doi.org/10.1038/SREP44097,.

[30] Wu Q, Zhang J, Kumar S, et al. Resilient anatomy and local plasticity of naive and stress haematopoiesis. Nature 2024;627:839. https://doi.org/10.1038/s41586-024-07186-6.

[31] Mertens TF, Liebheit AT, Ehl J, et al. MarShie: a clearing protocol for 3D analysis of single cells throughout the bone marrow at subcellular resolution. Nat Commun 2024;15:1764. https://doi.org/10.1038/s41467-024-45827-6.

[32] Ogawa M, Matsuzaki Y, Nishikawa S, et al. Expression and function of c-kit in hemopoietic progenitor cells. Journal of Experimental Medicine 1991;174:63–71. https://doi.org/10.1084/JEM.174.1.63,.

[33] Chatterjee S, Basak P, Das P, et al. Primitive Sca-1 positive bone marrow HSC in mouse model of aplastic anemia: A comparative study through flowcytometric analysis and scanning electron microscopy. Stem Cells Int 2010;2010. https://doi.org/10.4061/2010/614395,.

[34] Kyle-Cezar F, Echevarria-Lima J, Goldenberg RCDS, Rumjanek VM. Expression of c-kit and Sca-1 and their relationship with multidrug resistance protein 1 in mouse bone marrow

mononuclear cells. Immunology 2007;121:122–8. https://doi.org/10.1111/J.1365-2567.2007.02547.X,.

[35] Spindler M, Mott K, Schulze H, Bender M. Rapid isolation of mature murine primary megakaryocytes by size exclusion via filtration. Platelets 2023;34. https://doi.org/10.1080/09537104.2023.2192289,.

[36] Corash L, Levin J, Mok Y, Baker G, McDowell J. Measurement of megakaryocyte frequency and ploidy distribution in unfractionated murine bone marrow - PubMed. Exp Hematol 1989;17:278–86.

[37] Gorelashvili MG, Angay O, Hemmen K, Klaus V, Stegner D, Heinze KG. Megakaryocyte volume modulates bone marrow niche properties and cell migration dynamics. Haematologica 2020;105:895–904. https://doi.org/10.3324/HAEMATOL.2018.202010,.

[38] Gomariz A, Helbling PM, Isringhausen S, et al. Quantitative spatial analysis of haematopoiesis-regulating stromal cells in the bone marrow microenvironment by 3D microscopy. Nat Commun 2018;9. https://doi.org/10.1038/S41467-018-04770-Z,.

[39] Pinho S, Frenette PS. Haematopoietic stem cell activity and interactions with the niche. Nat Rev Mol Cell Biol 2019;20:303–20. https://doi.org/10.1038/S41580-019-0103-9,.

[40] Iida R, Welner RS, Zhao W, et al. Stem and progenitor cell subsets are affected by JAK2 signaling and can be monitored by flow cytometry. PLoS One 2014;9. https://doi.org/10.1371/JOURNAL.PONE.0093643,.

[41] Zhan H, Ma Y, Lin CHS, Kaushansky K. JAK2 V617F -mutant megakaryocytes contribute to hematopoietic stem/progenitor cell expansion in a model of murine myeloproliferation. Leukemia 2016;30:2332–41. https://doi.org/10.1038/LEU.2016.114,.

[42] Xing S, Ho WT, Zhao W, et al. Transgenic expression of JAK2V617F causes myeloproliferative disorders in mice. Blood 2008;111:5109–17. https://doi.org/10.1182/BLOOD-2007-05-091579,.

[43] Marty C, Lacout C, Martin A, et al. Myeloproliferative neoplasm induced by constitutive expression of JAK2 V617F in knock-in mice. Blood 2010;116:783–7. https://doi.org/10.1182/BLOOD-2009-12-257063,.

[44] Tiedt R, Hao-Shen H, Sobas MA, et al. Ratio of mutant JAK2-V617F to wild-type Jak2 determines the MPD phenotypes in transgenic mice. Blood 2008;111:3931–40. https://doi.org/10.1182/BLOOD-2007-08-107748,.

[45] Li J, Spensberger D, Ahn JS, et al. JAK2 V617F impairs hematopoietic stem cell function in a conditional knock-in mouse model of JAK2 V617F-positive essential thrombocythemia. Blood 2010;116:1528–38. https://doi.org/10.1182/BLOOD-2009-12-259747,.

[46] Zhao M, Perry JM, Marshall H, et al. Megakaryocytes maintain homeostatic quiescence and promote post-injury regeneration of hematopoietic stem cells. Nat Med 2014;20:1321–6. https://doi.org/10.1038/NM.3706,.

[47] Bruns I, Lucas D, Pinho S, et al. Megakaryocytes regulate hematopoietic stem cell quiescence through CXCL4 secretion. Nat Med 2014;20:1315–20. https://doi.org/10.1038/NM.3707,.

[48] Zhang Y, Lin CHS, Kaushansky K, Zhan H. JAK2V617F Megakaryocytes Promote Hematopoietic Stem/Progenitor Cell Expansion in Mice Through Thrombopoietin/MPL Signaling. Stem Cells 2018;36:1676–84. https://doi.org/10.1002/STEM.2888,.

[49] Khatib-Massalha E, Méndez-Ferrer S. Megakaryocyte Diversity in Ontogeny, Functions and Cell-Cell Interactions. Front Oncol 2022;12:840044. https://doi.org/10.3389/FONC.2022.840044/FULL.

[50] Hoermann G, Cerny-Reiterer S, Herrmann H, et al. Identification of oncostatin M as a JAK2 V617F-dependent amplifier of cytokine production and bone marrow remodeling in myeloproliferative neoplasms. The FASEB Journal 2012;26:894–906. https://doi.org/10.1096/FJ.11-193078,.

[51] Marty C, Lacout C, Droin N, et al. A role for reactive oxygen species in JAK2 V617F myeloproliferative neoplasm progression. Leukemia 2013;27:2187–95. https://doi.org/10.1038/LEU.2013.102,.

[52] Rai S, Grockowiak E, Hansen N, et al. Inhibition of interleukin-1β reduces myelofibrosis and osteosclerosis in mice with JAK2-V617F driven myeloproliferative neoplasm. Nat Commun 2022;13. https://doi.org/10.1038/S41467-022-32927-4,.

[53] Jutzi JS, Kleppe M, Dias J, et al. LSD1 inhibition prolongs survival in mouse models of mpn by selectively targeting the disease clone. Hemasphere 2018;2. https://doi.org/10.1097/HS9.0000000000000054,.

[54] Schaefer BC, Schaefer ML, Kappler JW, Marrack P, Kedl RM. Observation of antigen-dependent CD8+ T-cell/dendritic cell interactions in vivo. Cell Immunol 2001;214:110–22. https://doi.org/10.1006/CIMM.2001.1895,.

[55] Jordan CT, Astle CM, Zawadzki J, Mackarehtschian K, Lemischka IR, Harrison DE. Long-term repopulating abilities of enriched fetal liver stem cells measured by competitive repopulation. Exp Hematol 1995;23:1011–5.

[56] Morrison SJ, Hemmati HD, Wandycz AM, Weissman IL. The purification and characterization of fetal liver hematopoietic stem cells. Proc Natl Acad Sci U S A 1995;92:10302. https://doi.org/10.1073/pnas.92.22.10302.

[57] Rebel VI, Miller CL, Eaves CJ, Lansdorp PM. The Repopulation Potential of Fetal Liver Hematopoietic Stem Cells in Mice Exceeds That of Their Adult Bone Marrow Counterparts. Blood 1996;87:3500–7. https://doi.org/10.1182/blood.v87.8.3500.bloodjournal8783500.

[58] Gudmundsson KO, Stull SW, Keller JR. Transplantation of Mouse Fetal Liver Cells for Analyzing the Function of Hematopoietic Stem and Progenitor Cells. Methods Mol Biol 2012;879:123. https://doi.org/10.1007/978-1-61779-815-3_8.

[59] Staehle HF, Heinemann J, Gruender A, Omlor AM, Pahl HL, Jutzi JS. Jmjd1c is dispensable for healthy adult hematopoiesis and Jak2V617F-driven myeloproliferative disease initiation in mice. PLoS One 2020;15. https://doi.org/10.1371/JOURNAL.PONE.0228362,.

[60] Clutter MR, Heffner GC, Krutzik PO, Sachen KL, Nolan GP. Tyramide signal amplification for analysis of kinase activity by intracellular flow cytometry. Cytometry Part A 2010;77:1020–31. https://doi.org/10.1002/CYTO.A.20970,.

[61] Yamauchi K, Okamoto S, Ishida Y, et al. Fluorochromized tyramide-glucose oxidase as a multiplex fluorescent tyramide signal amplification system for histochemical analysis. Sci Rep 2022;12. https://doi.org/10.1038/S41598-022-19085-9,.

[62] Bankhead P, Loughrey MB, Fernández JA, et al. QuPath: Open source software for digital pathology image analysis. Scientific Reports 2017 7:1 2017;7:1–7. https://doi.org/10.1038/s41598-017-17204-5.

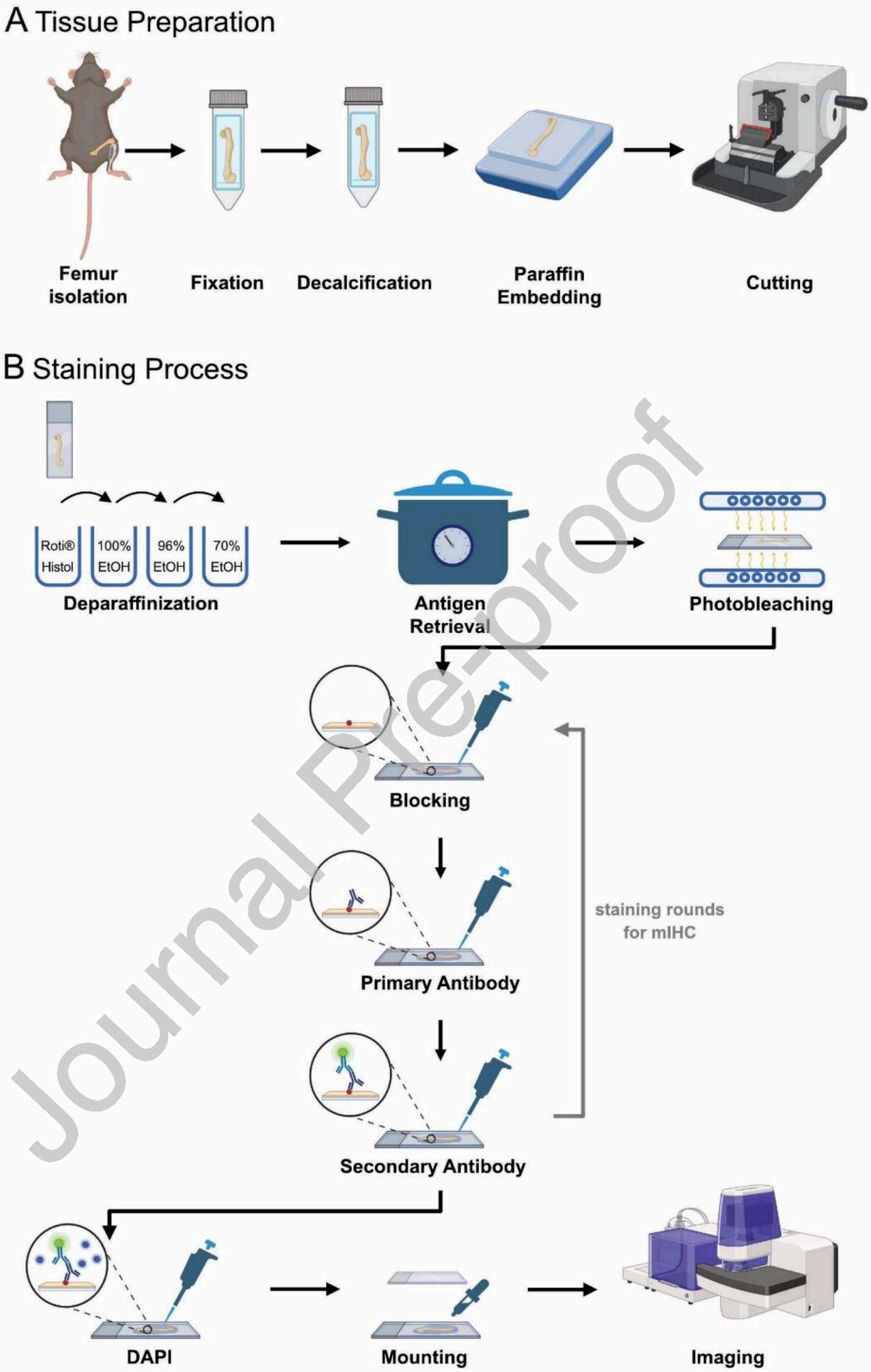

Figure 1: Workflow for tissue preparation and staining. (**A**) Tissue preparation involves femur isolation, fixation, decalcification, paraffin embedding, and sectioning using a microtome. (**B**) Tissue sections are subjected to deparaffinization, antigen retrieval, photobleaching, and blocking. Subsequently, they are stained with a target-

specific primary antibody followed by a secondary antibody. In immunofluorescence, the secondary antibody is conjugated to a fluorophore, while in multiplex immunohistochemistry (mIHC), the secondary antibody is conjugated to the horseradish peroxidase (HRP), which catalyzes a tyramide signal amplification (TSA) reaction. Multiplex immunohistochemistry (mIHC) uses multiple staining rounds to enable the detection of various markers. After nuclear staining with DAPI, the slides are mounted to preserve the stained sections for imaging. Created in BioRender. Pahl, H. (2026) https://BioRender.com/2kxhfb9.

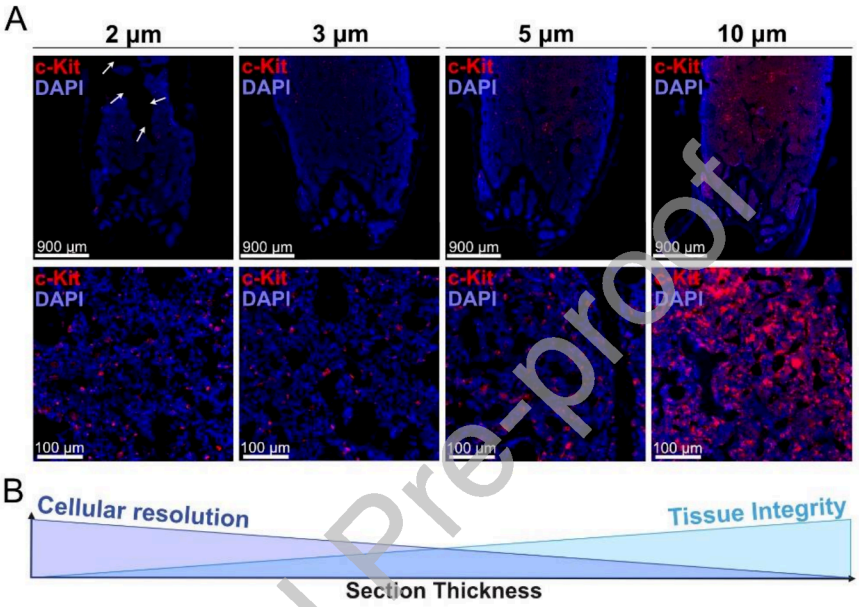

Figure 2: An optimal section thickness is required for high quality images. (**A**) Representative images of 2, 3, 5 or 10 µm sections of a paraffin-embedded murine femur derived from a wild-type mouse fixed in 4% paraformaldehyde for 2 hours are shown. Antigen retrieval was performed in pH 9 antigen retrieval buffer for 5 minutes and slides were stained with an antibody against c-Kit and a secondary anti-rabbit antibody conjugated to the Alexa Fluor 647 fluorophore as well as with DAPI. White arrows indicate fissures in the 2 µm section. (**B**) Schematic illustration of the impact of section thickness on tissue integrity and cellular resolution.

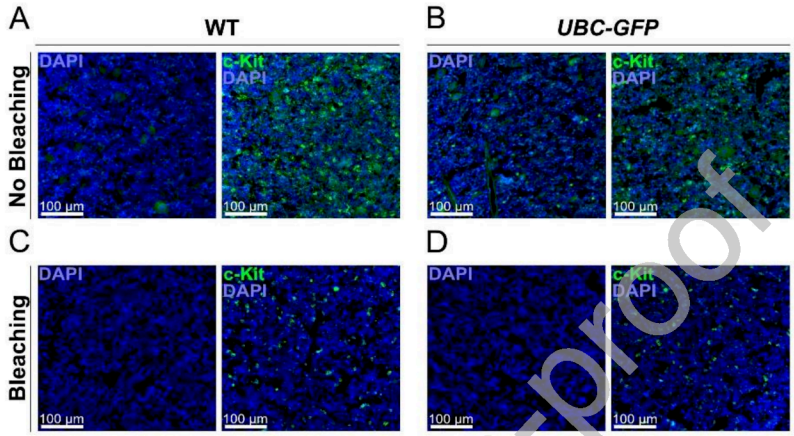

Figure 3: Photobleaching improves signal specificity of murine bone marrow sections. (**A-D**) Representative images of 3 µm sections of paraffin-embedded murine femora derived from (**A+C**) a wild-type or (**B+D**) a *UBC-GFP* mouse, fixed in 4% paraformaldehyde for 2 hours. Antigen retrieval was performed in pH 9 antigen retrieval

buffer for 5 minutes. (**A+B**) Unbleached and (**C+D**) bleached sections were stained with DAPI alone (left) or with DAPI, a primary antibody against c-Kit, and a secondary anti-rabbit antibody conjugated to the Alexa Fluor 488 fluorophore (right).

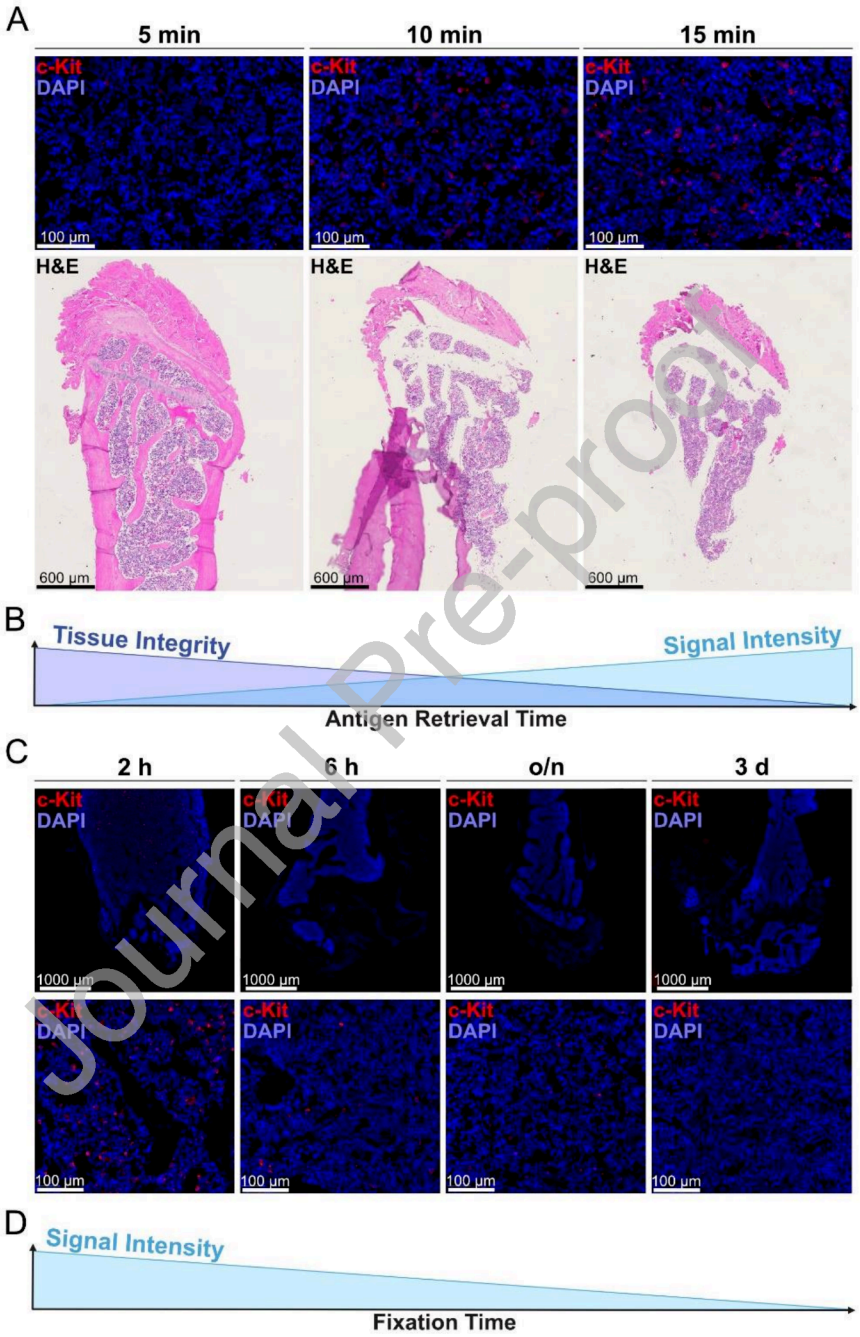

Figure 4: Short fixation combined with mild antigen retrieval provides the best staining quality of murine bone marrow sections. (**A**) Representative images of 3 µm sections of a paraffin-embedded murine femur derived from a wild-type mouse fixed in 4% paraformaldehyde overnight (o/n). Antigen retrieval was performed in pH 9

antigen retrieval buffer for 5 (left), 10 (middle) or 15 (right) minutes. Top: Staining with DAPI and an antibody against c-Kit. Bottom: H&E staining. (**B**) Schematic illustration of the impact of antigen retrieval time on tissue integrity and signal intensity. (**C**) Representative images of 3 µm sections of a paraffin-embedded murine femur fixed in 4% paraformaldehyde for 2 hours, 6 hours, o/n or 3 days, as indicated. Antigen retrieval was performed for 5 minutes in pH 9 antigen retrieval buffer. Staining with DAPI, an antibody against c-Kit, and a secondary anti-rabbit antibody conjugated to the Alexa Fluor 647 fluorophore. (**D**) Schematic illustration of the impact of paraformaldehyde fixation time on signal intensity.

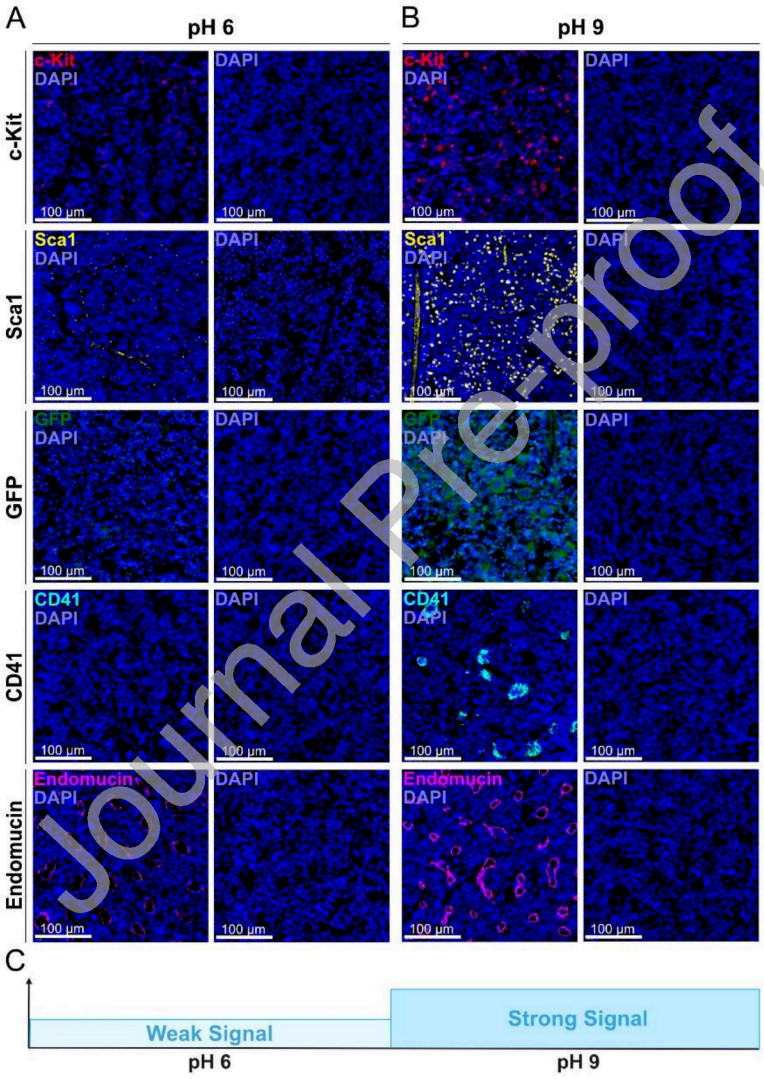

Figure 5: pH 9 antigen retrieval buffer provides optimal staining quality for murine bone marrow sections. (**A+B**) Representative images of 3 µm sections of murine paraffin-embedded femora, fixed in 4%

paraformaldehyde for 2 hours, were used to test antigen retrieval with (**A**) pH 6 or (**B**) pH 9 buffers. Antigen retrieval was performed for 5 minutes. (**A+B**) Left: Staining with DAPI and an antibody against c-Kit, Sca1, GFP, CD41 and endomucin as indicated. Depending on the species of the primary antibody, either an anti-rabbit Alexa Fluor 647 or an anti-rat Alexa Fluor 568 secondary antibody was used. The colors shown in the panels are assigned as pseudocolors. Right: Control staining with DAPI and the secondary antibody only. Sections from a wild-type mouse were used for c-Kit, Sca-1, CD41, and endomucin staining, while sections from a *UBC-GFP* mouse were used for GFP staining. (**C**) Schematic illustration of the impact of antigen retrieval pH on tissue integrity and signal intensity.

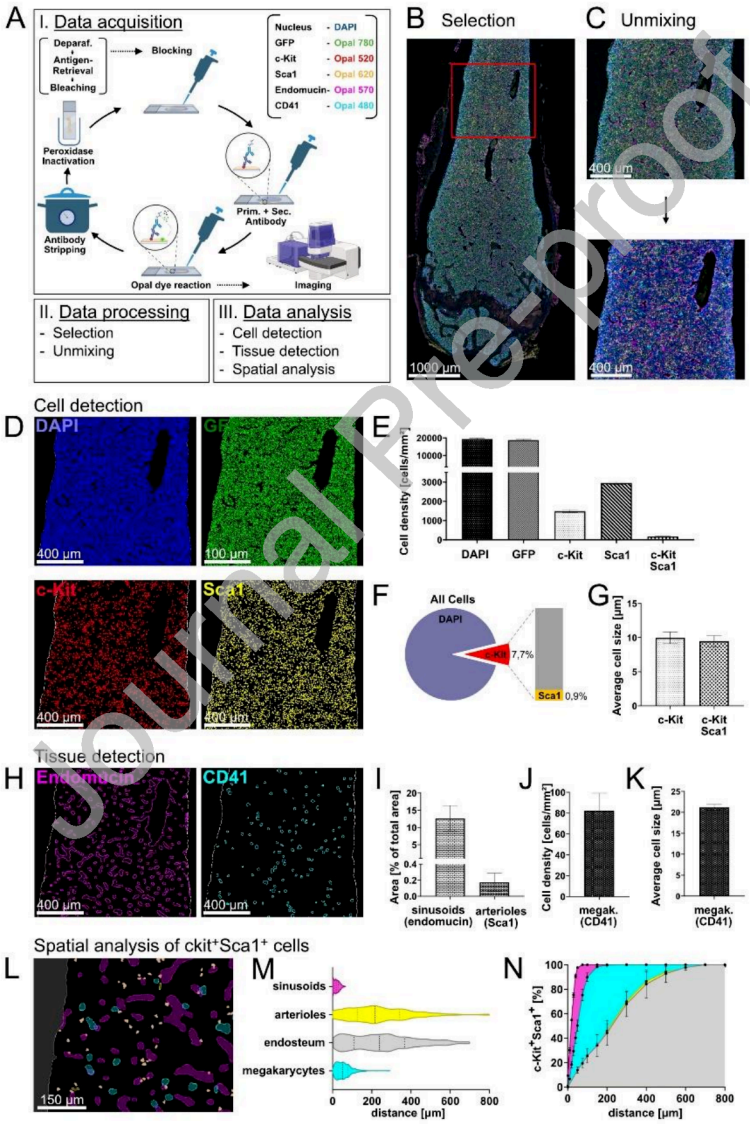

Figure 6: Multiplex immunohistochemistry staining of key bone marrow niche components using the Akoya technology. (**A**) Workflow for data acquisition (I), processing (II) and analysis (III). Created in BioRender. Pahl, H. (2026) https://BioRender.com/2kxhfb9. (**B-N**) 3 µm sections of paraffin-embedded femora from mice transplanted with *UBC-GFP* donor cells were examined. The sections were fixed in 4% paraformaldehyde for 2 hours and stained with DAPI and antibodies against the following markers: GFP (Opal 780), c-Kit (Opal 520), Sca1 (Opal 620), endomucin (Opal 570), and CD41 (Opal 480). (**B+C**) Data processing includes (**B**) selection of a region of interest and (**C**) spectral unmixing. (**D-N**) Data analysis includes (**D-G**) cell detection, (**H-K**) tissue detection, and (**L-N**) spatial analysis: (**D**) Cell mask of stained cells created using the Cell Detection tool in QuPath. The DAPI (top, left), GFP (top, right), c-Kit (bottom, left) and Sca1 (bottom, right) signals are shown. (**E**) Average cell density quantified based on the DAPI, GFP, c-Kit and Sca1 signals. (**F**) Frequency of c-Kit$^+$ (7.7%) and c-Kit$^+$/Sca1$^+$ (0.9%) cells by DAPI staining. (**G**) Average cell size of c-Kit$^+$ and c-Kit$^+$/Sca1$^+$ cells. (**H**) Segmentation mask of the stained tissues created using the Pixel Classifier tool in QuPath. The endomucin (left) and CD41 (right) signals are shown. (**I**) Area covered by sinusoids and arterioles. (**J+K**) Average (**J**) cell density and (**K**) size of CD41$^+$ megakaryocytes. (**L**) Overlaid cell and tissue detection masks showing c-Kit$^+$/Sca1$^+$ cells (orange), CD41$^+$ megakaryocytes (turquoise), sinusoids (purple), arterioles (yellow), and the endosteal bone surface (gray). (**M+N**) Spatial analysis depicted as a (**M**) violin plot and (**N**) a cumulative distribution plot showing the distance of c-Kit$^+$/Sca1$^+$ cells from megakaryocytes (turquoise), sinusoids (purple), arterioles (yellow), or the endosteal bone surface (gray), respectively. (**E,G,I-K**) Mean and SEM are shown. n=3 mice (**B+C+D+H+L**) Representative images are shown.

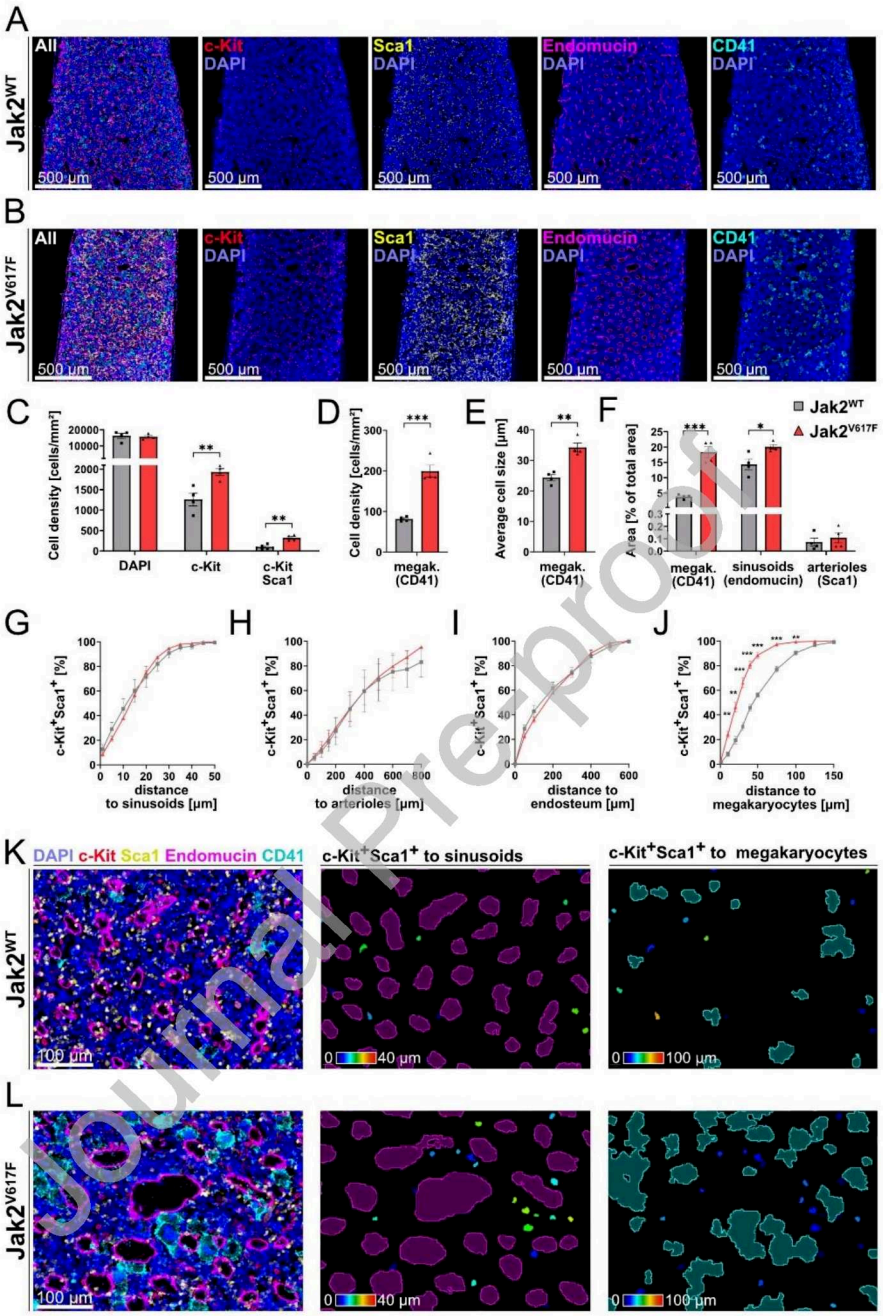

Figure 7: Jak2^{V617F} mice display an altered megakaryocytic bone marrow niche. (**A-L**) 3 µm sections of paraffin-embedded murine femora were examined. The sections were fixed in 4% paraformaldehyde for 2 hours and stained with DAPI as well as antibodies against the following markers: c-Kit (Opal 520), Sca1 (Opal 620), endomucin (Opal 570), and CD41 (Opal 480). (**A+B**) Unmixed multiplex images of femoral sections from (**A**) a littermate control mouse and (**B**) a Jak2^{V617F} mouse. The merged signals (top, left), DAPI (top, right), c-Kit (middle,

left), Sca1 (middle, right), CD41 (bottom, left), and endomucin (bottom, right) are shown. (**C**) Average cell density based on the DAPI, c-Kit and merged c-Kit/Sca1 signals. (**D+E**) Average (**D**) cell density and (**E**) size of $CD41^+$ megakaryocytes. (**F**) Area covered by megakaryocytes, sinusoids, and arterioles. (**G-J**) Cumulative distribution plots showing the distance of $c\text{-}Kit^+/Sca1^+$ cells towards (**G**) sinusoids, (**H**) arterioles, (**I**) the endosteal bone surface, and (**J**) megakaryocytes. (**K+L**) Merged c-Kit, Sca1, and CD41 signals (left) and corresponding measurement maps showing the distance of $c\text{-}Kit^+/Sca1^+$ cells to megakaryocytes (right) of (**K**) control ($Jak2^{WT}$) and (**L**) $Jak2^{V617F}$ mice. (**C-J**) Statistical analyses by unpaired Student's *t*-tests. n=4 per genotype. *p<0.05, **p<0.01, ***p<0.001. Mean and SEM are shown. (**A+B+K+L**) Representative images are shown.

Acknowledgement

The authors thank Martina de Groot for her expert technical assistance. The authors appreciate the technical support by the Lighthouse Core Facility, namely by Marie Follo, Elitsa Bodurova, Michael Selle, Dieter Herchenbach, Jan Bodinek, Urmila Gopakumar and as well as by the veterinary staff, namely by Natalie Krause, Alexandra Bonk, Claudia Bravo Almendarez and Sabrina Schenk. H.F.S. was funded by Else Kröner-Fresenius-Stiftung (2021_EKEA.122). H.L.P. was supported by grants from the Deutsche Forschungsgemeinschaft (DFG), Pa 611/5-3, Pa 611/9-2 and Pa 611/11-1, Project 3 of the DFG Research-Unit TARGET-MPN. H.F.S. is a fellow in the EXCEL clinician-scientist program at the University of Freiburg Medical Faculty, funded by the Else Kröner-Fresenius-Stiftung, granted to H.L.P. (2016_Kolleg_15). H.F.S. is also a fellow in the DGIM clinician-scientist program, funded by the German Society of Internal Medicine (DGIM). F.Z., A.M., E.E., and F.P. were supported by the MOTI-VATE scholarship program of the Medical Faculty Freiburg. K.G. and P.E. were supported by the "Peter-Scriba Doctoral Scholarship" awarded by the DGIM. S.K. was supported by the "Mildred Scheel Doctoral Program" of the German Cancer Aid (Deutsche Krebshilfe).

Authors' Contributions

F.Z. designed research, performed research, analyzed data, wrote the paper

K.G. performed research, analyzed data

A.G. designed research, performed research, supervised research, analyzed data

P.E. performed research, analyzed data

A.M. performed research, analyzed data

J.S. performed research, analyzed data

F.P. performed research, analyzed data

A.G. performed research, analyzed data

C.K. designed research, analyzed data

A.M.S. performed research, analyzed data

S.B.K. performed research, analyzed data

S.K. performed research, analyzed data

E.E. designed research, analyzed data

C.R.O. designed research, analyzed data, supervised research

L.I. designed research, contributed vital reagents, edited the paper

H.L.P. designed research, supervised research, wrote the paper

H.F.S. designed research, performed research, analyzed data, supervised research, wrote the paper

Competing interests

The authors declare no competing interests.

Table 1. Comparison of different staining protocols for murine bone specimens

Technique	**mIHC**	**CODEX**	**Whole-mount**	**Clearing**
Study	This study	Karnik et al.[11]	Wu et al.[30]	Mertens et al. [31]
Tissue	FFPE	cryosections	fresh samples	fresh samples
Spatial resolution	2D (3 µm)	2D/3D (10 µm)	3D (35 µm)	3D (400 µm)
Multiplexing capacity	7 markers	25-50 markers	4-6 markers	4 markers

Teaser Abstract

Processing murine femora for immunofluorescence staining poses considerable challenges, and a standardized workflow has not yet been systematically described. In this study, we optimized tissue preparation for murine formalin-fixed, paraffin-embedded femur sections and established an efficient multiplex protocol enabling spatial analysis of hematopoietic stem and progenitor cells within the bone marrow niche. Applying this panel to femur sections from $Jak2^{V617F}$ mice, we observed specific alterations in the megakaryocytic niche, underscoring our method's utility for detecting spatial features relevant to hematopoietic disease.